Scripta Materialia 197 (2021) 113783

Contents lists available at ScienceDirect

Scripta Materialia

journal homepage: www.elsevier.com/locate/scriptamat

3D mapping of orientation variation and local residual stress within individual grains of pearlitic steel using synchrotron dark field X-ray microscopy

C. Yildirim[a,*], C. Jessop[b], J. Ahlström[b], C. Detlefs[a], Y. Zhang[c,*]

[a] European Synchrotron Radiation Facility, 71 Avenue des Martyrs, Grenoble 38043, France
[b] Department of Industrial and Materials Science, Chalmers University of Technology, Gothenburg 412 96, Sweden
[c] Department of Mechanical Engineering, Technical University of Denmark, 2800 Kgs., Lyngby, Denmark

ARTICLE INFO

Article history:
Received 11 November 2020
Revised 14 January 2021
Accepted 29 January 2021
Available online 11 February 2021

Keywords:
Pearlitic steels
Synchrotron radiation
X-ray diffraction (XRD)
Residual stresses

ABSTRACT

Assessing the local residual stress and orientation with nanometer resolution within embedded steel grains has remained challenging. Here we use an advanced synchrotron technique, dark field X-ray microscopy to map 3D lattice variations, including both the crystallographic orientation and lattice strain, within two pro-eutectoid ferrite grains in pearlitic steel. We found an orientation variation up to 0.5° and compressive elastic strain up to 1.8×10^{-3} are present in the as-manufactured sample. There is no direct correlation between the measured compressive strain and lattice orientation. The origin of the variations and their influence on the manufacturing process and mechanical properties are discussed.

Medium-carbon hypoeutectoid steel with a predominantly pearlitic microstructure is an attractive engineering material used widely in the modern society, owing to its good wear resistance and balance in strength and ductility. Example applications of this class of materials are wheels and rails in railway industry [1–3]. Microscopically, this type of steel consists typically of some relatively soft pro-eutectoid ferrite, which contributes to the good ductility, and relatively hard pearlite, composed of alternate fine-spaced lamellae of cementite and ferrite, which contribute to the high strength. Due to the presence of two phases, cementite and ferrite, local residual stresses can develop within cementite and ferrite during manufacturing or in service. These stresses can be detrimental for the wear and fatigue properties of the steel, as it may lead to stress concentration and thus crack initiation at e.g. interfaces between pearlite and pro-eutectoid ferrite, as experimentally observed [4]. To optimize the performance of the steel, it is therefore desired to determine the *level* and *distribution* of the local residual stresses and relate them to the local microstructure.

Experimentally, it is however extremely challenging to measure the residual stresses locally at micron- to submicron scale. Previous studies using high resolution electron backscattered diffraction (EBSD) (Wilkinson's method) have shown the presence and the heterogeneous distribution of the local residual stress [5,6]. However, EBSD measurements are conducted at the free sample surface, where the stress state may be different from that in the bulk as stresses rearrange and relax on cutting since a free surface cannot carry stress. During the last 20 years, several synchrotron X-ray techniques, including three dimensional X-ray diffraction (3DXRD) [7,8], have been developed for non-destructive 3D characterization of microstructure and elastic strains (from which stress can be derived) in the bulk. Very recently an emerging technique, dark field X-ray microscopy (DFXM), has been developed as an extension of the 3DXRD for high resolution orientation and strain mapping [9–11]. By utilizing compound refractive **lenses** (CRLs) to magnify the diffracted X-ray beam, an angular, spatial, and strain resolution of 0.005°, sub-100 nm and 5×10^{-5} respectively, can be achieved at the present stage [12–14].

Here we use DFXM for the characterization of local orientation variation and strain distribution within individual fully embedded *3D* grains in a pearlitic steel sample. This is the first time that the local residual strains have been measured in 3D experimentally for pearlitic steel. The results will shed a light on the understanding of the development of microstructure during manufacturing and their impact on the post mechanical properties.

The steel used in this study was ER8 grade wheel steel. This material follows the standard EN 13262 [15]. The nominal chemical composition of the material is listed in Table 1. This steel has undergone standard rim chilling heat treatment (cooled with wa-

* Corresponding authors at: European Synchrotron Radiation Facility CS 40220 71, avenue des Martyrs, Grenoble F-38043, France.
E-mail addresses: can.yildirim@esrf.fr (C. Yildirim), yubz@dtu.dk (Y. Zhang).

https://doi.org/10.1016/j.scriptamat.2021.113783
1359-6462/

Table 1
Chemical composition of the studied pearlitic steel, in wt%.

C	Si	Mn	Mo	Cr	Ni	S	P	V	Fe
0.56	0.40	0.80	0.08	0.30	0.30	0.015	0.020	0.06	Bal.

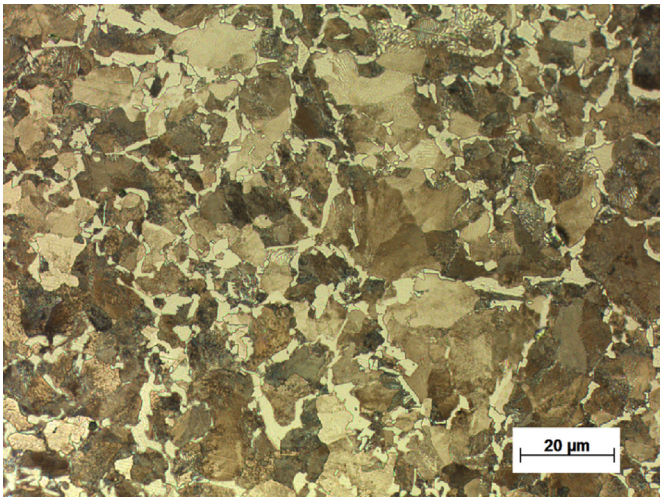

Fig. 1. Optical micrograph showing the microstructure of the pearlitic wheel steel ER8 grade.

ter jets after high temperature austenitization), which creates a fine-pearlitic microstructure (see Fig. 1) consisting of 7-10% of pro-eutectoid ferrite (appearing bright in Fig. 1) in a pearlite matrix (darker areas in Fig. 1). The grain size of the pro-eutectoid ferrite grains is about 5-10 µm, while the size of the pearlitic colonies is in the range of 10-20 µm. The interlamellar spacing of the pearlite is around 150-160 nm [2]. A thin slice of 200 µm was prepared for synchrotron DFXM experiments. To avoid introducing artificial or removing existing local internal stresses, the sample was cut by electrical discharge machining and electropolished after careful mechanical polishing.

The DFXM experiments were carried out at the beamline ID06 at the European Synchrotron Facility (ESRF) [16]. Fig. 2(a) shows a sketch of the experimental set-up. For the measurements, 17 keV photons with a 10^{-4} bandwidth were selected by a Si (111) Bragg-Bragg double crystal monochromator situated 35.8 m from a cryogenic permanent magnet undulator source. To focus the incoming X-ray, a 2D transfocator with 8 Be CRLs and a 1D condenser with 58 Be lenses were used. To magnify the diffracted beam, a 2D objective of 88 Be lenses was placed at 268 mm away from the sample (see Fig. 2). The effective magnification is about 18.67 which results in a final spatial resolution of 75 nm/pixel in horizontal and 197nm/pixel in vertical directions when combined with the optical elements of the detector. A 1D focused line beam having a profile of 400 $\times$ 1 μm^2 (horizontal x vertical) was used to illuminate the sample for recording section topography images [17]. A 2D CCD detector having 47 µm pixel size located 180 mm downstream of the sample was used to record the 110 diffraction ring for grain selection prior to DFXM scans (see Fig. 2(b) and more in the attached video). We believe that the bright spots in the diffraction ring with a narrow angular width have their origin in pro-eutectoid ferrite grains. Two of these, referred to as Grain 1 and Grain 2, were selected for DFXM scans. The orientation of their 110 Bragg planes, $\vec{Q}_{110}$, differs by less than 7°.

For the mapping of local orientation variations, referred to as mosaicity scans throughout, the sample was tilted around Y and X axes, referred to as θ and η rotations, respectively (see Fig. 2(a)). To map the relative axial strain, a combination of sample, objective and camera motions were performed. The resulting angular resolution of the experimental setup was 0.008°, 0.016°, and 0.057° in θ, η, and 2θ, respectively. In order to obtain 3D data of the selected grains, the sample was moved in the vertical direction to scan 11 equidistant layers covering 10 and 16 µm distances for Grain 1 and Grain 2, respectively. The mosaicity scans covered 0.4° in 20 steps in θ rotation and 0.6° in 30 steps in η rotation for both grains. The strain scans were measured in 24 steps over 0.12° in 2θ for Grain 1 and 15 steps over 0.1° in 2θ for Grain 2, respectively. The axial strain was determined using Eq. (1):

$$\varepsilon = \frac{d - d_0}{d_0} \simeq -(\Delta\theta)/\tan\theta, \quad (1)$$

where d and d_0 are plane spacing for strained and strain-free crystal lattices, and $\Delta\theta = \theta\text{-}\theta_0$ (θ_0 corresponding to the diffraction angle for the unstrained case). In the present study, a strain-free lattice parameter of a_0= 2.8673 Å was used for the calculation. This parameter was estimated based on the chemical composition (see Table 1) using a function that was deduced based on various publications [18].

To evaluate the DFXM data, we examined the intensity at a pixel coordinate as function of the goniometer and objective angles across the scan. 2D maps of relative orientation and strain maps were generated using a method described in Ref. [9]. The DFXM results for Grain 1 and Grain 2 on all the scanned 2D sections are shown in Fig. 3 and Fig. S1, respectively. The mosaicity (orientation spread) maps in the top row of Fig. 3 reveal a local orientation change (pole figure) of a single grain rather than a complete 3-parameter orientation. A local reference orientation is defined by the centre of mass of the grain, in accordance with our previous work [13,19]. The mosaicity maps show distinct sub-domains (sub-grains) of similar orientation inside the ferrite grain. The misorientation between neighbouring subgrains is about 0.1-0.2° (see the middle row in Fig. 3), and the average misorientation, defined as the mean of the misorientation angles between all pairs of nearest neighbour pixels within each layer, is about 0.126 $\pm$ 0.017°. The maximum orientation difference within the grain is about 0.5°. Similar result is seen for Grain 2, except that there is also a systematic orientation change from the first slice to last slice (see Table 2 and Fig. S1 in the supplementary materials).

The spatial distribution of elastic strain for Grain 1 on all the scanned 2D sections is shown in the bottom row of Fig. 3. The elastic strain values are mainly negative (see Figs. 3 and 4), meaning compressive axial strains. The strains are inhomogeneously distributed within the grain, both within each slice and between different slices. Although there is a continuous strain gradient from positive to negative values, no systematic change of microstructural features from one side (the first slice) to the other side (the last slice) of the grain is seen. The strain gradient may have its origin from the neighbouring pearlite grains. There are some distinct local sub-domains with similar strain values. The correlation between the orientation variation and strain sub-domains is, however, weak except for the layers in the centre of the grain. Similar results are seen for Grain 2 (see Fig. S1 in the supplementary materials). Notice that the shapes of some slices of the grain are different when comparing mosaicity and strain maps. This is due to the different scan ranges that do not fully cover the diffraction conditions for all parts of the grain. The orientation distribution (θ- η) covers about 0.5° degrees in the angular space. Thus, some parts of the slices of the grain are out of the resolution window for strain scans which is a combination of (θ-2θ). This occurs due to the decoupling of the lattice parameter variation from the lattice orientation as observed recently for ceramic precipitates in maraging steel [19]**.** The total strain variation range within the grain is about 2-3 $\times$ 10^{-3} (see Fig. 4) for both grains.

The results show evidently the presence of residual stresses and stress variation within individual grains. The maximum compres-

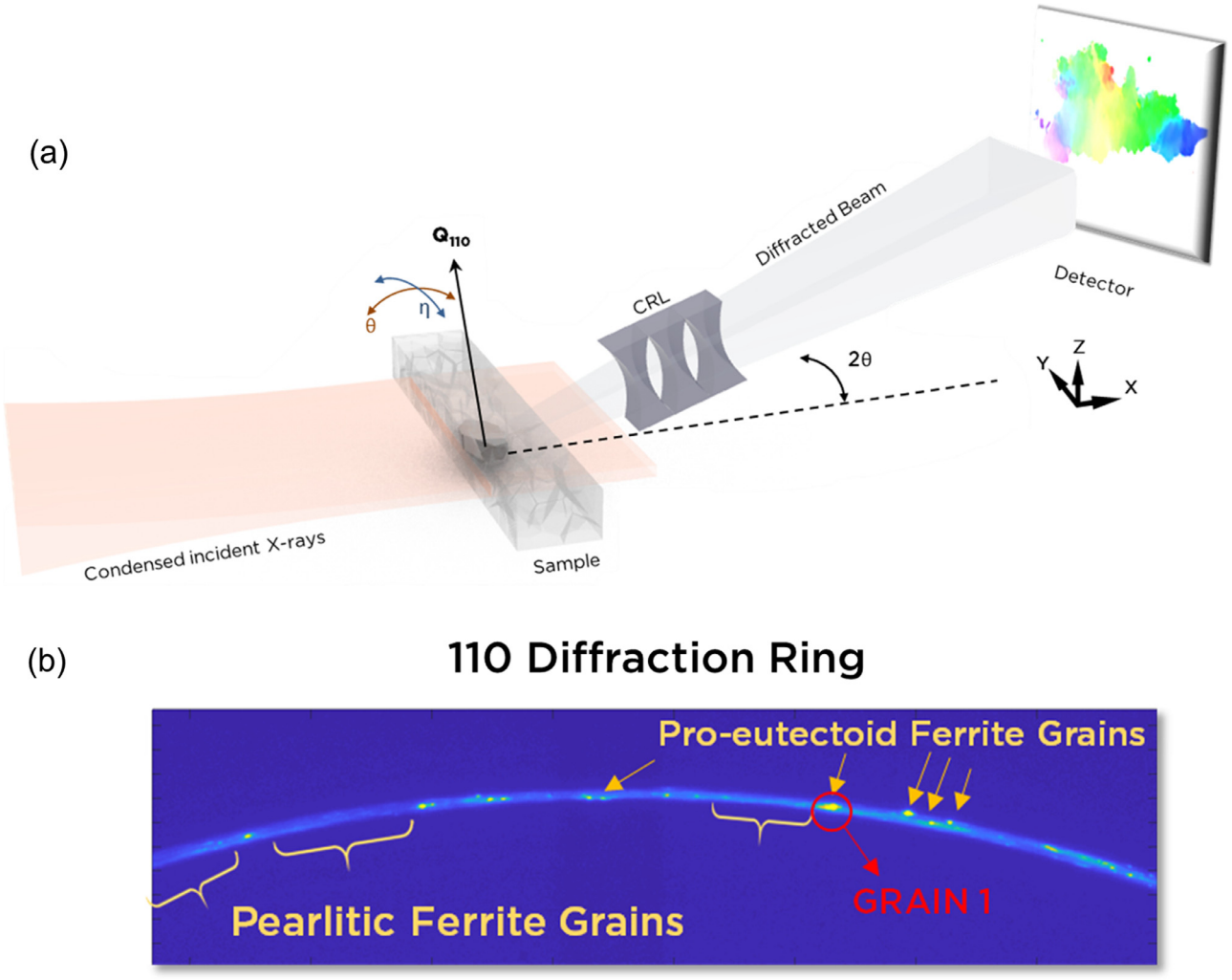

Fig. 2. (a) Schematic of the DFXM experimental setup. The incident beam was focused horizontally to illuminate slices of the diffracting grain (shown in dark). The angles θ, η, and 2θ correspond to the tilt angles around the $\vec{\boldsymbol{Q}}_{110}$ scattering vector of the grain of interest. An objective CRL was used to create a magnified image of the grain at about 5 meters away from the sample. (b) A ~30° portion of 110 diffraction ring showing powder diffraction-like regions (pearlitic ferrite grains with high mosaicity) and bright spots (pro-eutectoid ferrite with narrow angular spread). Brighter colors show higher detected intensity.

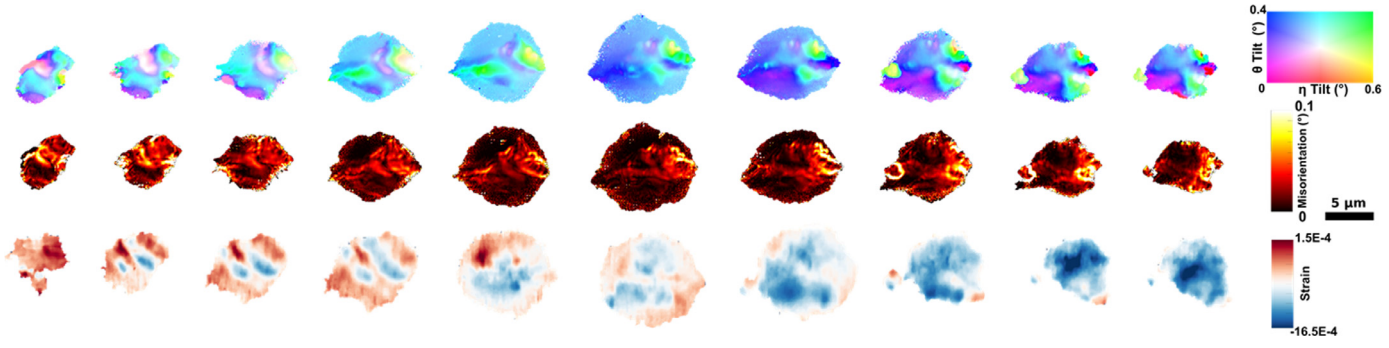

Fig. 3. Mosaicity and strain maps for all the scanned 2D sections of Grain 1. From top to bottom rows: mosaicity, misorientation and strain maps. The distance between the layers is about 600 nm. The reader is referred to the web version of this paper for the color representation of this figure. The color scales which are smaller than the exact scan ranges were chosen to enhance the relevant features in (b) and (c).

Table 2
Average misorientation and dislocation density within the two mapped grains.

	Average Misorientation (°)	ρ_{GND} (x 10^{14} m^{-2})
Grain 1	0.126 ± 0.017	2.36 ± 0.32
Grain 2	0.129 ± 0.020	2.42 ± 0.38

sive stress is estimated roughly to be about 300 MPa based on the maximum compressive strain and directional Young's modulus along [110]. Considering the reasons for the development of local residual stress, it is generally agreed that the residual stresses are developed during phase transformation because of the orientation and lattice differences between the ferrite and cementite [20].

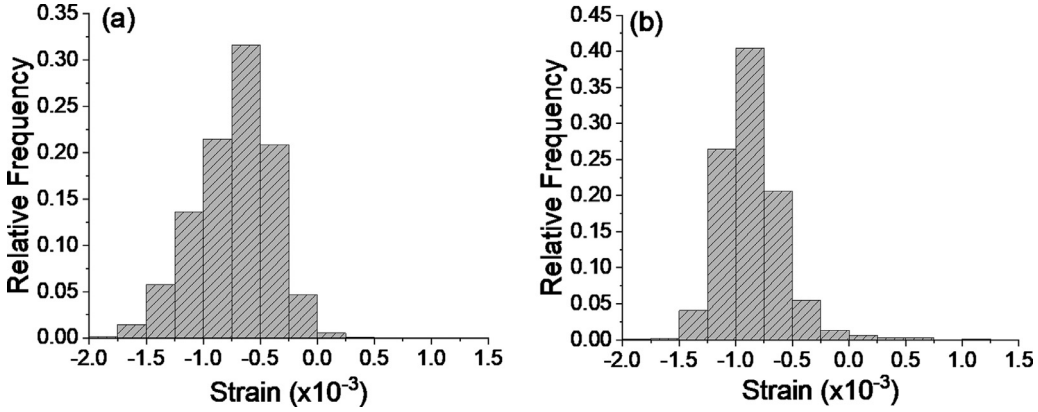

Fig. 4. Histogram showing the frequency distribution of elastic strain values for Grain 1 (a) and Grain 2 (b).

Table 3
Thermal expansion coefficient of cementite and ferrite [23].

	Thermal expansion coefficient ($10^{-5}K^{-1}$)	
	300-420°C	500- 640°C
Fe_3C	1.54	1.74
Ferrite	1.45	1.50

When austenite transforms to either ferrite or cementite, the volume of the unit cell **expands** [21], leading therefore to compressive stresses within the two phases, which agrees well the present results. The thermal stress due to the thermal expansion seen in other steel [22] should be small in this material, as the thermal expansion coefficients for ferrite and cementite are similar within the relevant temperature ranges (see Table 3) [23,24]. With the parameters in Table 3, a simple estimation using an analytical model [25] shows that the thermal stress is only in the order of a few MPa during cooling from 800°C to room temperature.

Water quench may also introduce some residual stress due to the temperature gradient in the sample [26]. But this stress is only on a macroscopic scale and will be released during sample preparation, as only a slice of 200 μm is used for the present study. However, water quench can lower the phase transformation temperature, and thus is coupled with the phase transformation induced stress [27]. It has been found that a lower phase transformation temperature results in a higher dislocation density and residual stress [20,28]. A quantitative understanding of the effects of water quench on the local stresses requires further studies where samples prepared under different cooling rates are involved, and will be of interest for future work.

The presence of orientation spread in the mapped grains implies that the residual stresses have been higher than the yield stress of the ferrite at certain stages during cooling, leading to plastic deformation and thereby relaxing part of the residual stresses. The dislocation densities within the mapped grains estimated from the average misorientation angles [29] are in the order of 10^{14} m^{-2} (see Table 2). This density is slightly higher than that within the ferrite lamellae in the pearlite colonies measured using transmission electron microcopy [2], which is about 6×10^{13} m^{-2}. This difference can be attributed to the surface relaxation effect due to the sample preparation for electron microscope studies [19]. The difference also suggests that the constraints from the lamellar structure of alternative ferrite and cementite may contribute additionally the development of local residual stresses.

According to the Taylor strengthening mechanism [30,31], the contribution of the dislocation density to the strength, σ, can be calculated as:

$$\sigma = \alpha M G b \sqrt{\rho} \quad (2)$$

where M is the Taylor factor, α is a constant, G is the shear modulus, and b is the Burgers vector. With $M \approx 3$, $\alpha \approx 0.24$, $b = 0.248$ nm and $G = 77$ GPa, a stress of 210 MPa is obtained for the present ferrite grains. Compared to the yield strength of this material, which is about 600 MPa, both the residual stress and the strength contribution from dislocations are significant and should be considered when the steel is annealed or deformed under external loading [32,33]. In addition, the level of the observed local residual stresses is similar to the macroscopic residual stresses developed due to the temperature gradients during cooling [34,35] or the external loading stresses that have been applied to control the phase transformation process [27,36]. Therefore, the local residual stresses need to be considered when developing advanced models for predicting the manufacturing process [21,26].

In the present study, the local variation of both orientation and elastic strain in 3D grains in pearlitic steel has been studied using an advanced synchrotron technique, dark field X-ray microscopy (DFXM). The results show the ability of DFXM for studying the local strains of engineering materials with high angular and strain resolution. We found that the elastic strains are mainly compressive and are locally heterogeneous within individual 3D ferrite grains, and the variations in elastic strain within individual grains can be as large as 2×10^{-3}. The results suggest that local residual stress should be considered when evaluating the mechanical properties of pearlitic steel.

In particular, measuring the strain and orientation relationships between the pearlitic lamellae is of significant interest. These measurements should be possible for further studies by exploiting the recent advancements in DFXM yielding ~30nm spatial resolution [37]. Coupling with a recently developed radiation furnace [38], DFXM will then be an ideal tool for studying microstructural engineering in eutectoid or near-eutectoid steels [27] .

Declaration of Competing Interest

The authors declare that they have no known competing financial interests or personal relationships that could have appeared to influence the work reported in this paper.

Acknowledgement

C.Y. thanks Onderzoeks Centrum voor de Aanwending van Staal (OCAS), Belgium, for the financial support of this project. This work has been a part of research activities within the Centre of Excellence CHARMEC (CHAlmers Railway MEChanics,

www.charmec.chalmers.se). Parts of the study has been funded within the European Union's Horizon 2020 research and innovation programme in the project In2Track2 under grant agreement No 826255. Y.Z. acknowledges the support from the European Research Council (ERC) under the European Union's Horizon 2020 research and innovation programme (grant agreement No 788567, M4D). Assoc Prof Fang Liu are acknowledged for careful sample preparation. Finally, the authors acknowledge the ESRF for provision of beamtime on ID06.

Supplementary materials

Supplementary material associated with this article can be found, in the online version, at doi:10.1016/j.scriptamat.2021.113783.

References

[1] D. Nikas, J. Ahlström, A. Malakizadi, Wear 366–367 (2016) 407–415.
[2] D. Nikas, X. Zhang, J. Ahlström, Mater. Sci. Eng. A 737 (2018) 341–347.
[3] K. Cvetkovski, J. Ahlström, B. Karlsson, Wear 271 (2011) 382–387.
[4] H.C. Eden, J.E. Garnham, C.L. Davis, Taylor & Francis, Influential microstructural changes on rolling contact fatigue crack initiation in pearlitic rail steels, Mater. Sci. Technol. 21 (6) (2005) 623–629.
[5] N. Koga, N. Nakada, T. Tsuchiyama, S. Takaki, M. Ojima, Y. Adachi, Scr. Mater. 67 (2012) 400–403.
[6] N. Nakada, N. Koga, T. Tsuchiyama, S. Takaki, Scr. Mater. 61 (2009) 133–136.
[7] J. Oddershede, S. Schmidt, H.F. Poulsen, L. Margulies, J. Wright, M. Moscicki, W. Reimers, G. Winther, Mater. Charact. 62 (2011) 651–660.
[8] H.F. Poulsen, J. Appl. Crystallogr. 45 (2012) 1084–1097.
[9] H. Simons, A. King, W. Ludwig, C. Detlefs, W. Pantleon, S. Schmidt, I. Snigireva, A. Snigirev, H.F. Poulsen, Nat. Commun. 6 (2015) 1–6.
[10] H. Simons, A.C. Jakobsen, S.R. Ahl, C. Detlefs, H.F. Poulsen, MRS Bull. 41 (2016) 454–459.
[11] S.R. Ahl, H. Simons, Y.B. Zhang, C. Detlefs, F. Stöhr, A.C. Jakobsen, D. Juul Jensen, H.F. Poulsen, Scr. Mater. 139 (2017) 87–91.
[12] H. Simons, A.B. Haugen, A.C. Jakobsen, S. Schmidt, F. Stöhr, M. Majkut, C. Detlefs, J.E. Daniels, D. Damjanovic, H.F. Poulsen, Nat. Mater. 17 (2018) 814–819.
[13] N. Mavrikakis, C. Detlefs, P.K. Cook, M. Kutsal, A.P.C. Campos, M. Gauvin, P.R. Calvillo, W. Saikaly, R. Hubert, H.F. Poulsen, A. Vaugeois, H. Zapolsky, D. Mangelinck, M. Dumont, C. Yildirim, Acta Mater. 174 (2019) 92–104.
[14] H.F. Poulsen, A.C. Jakobsen, H. Simons, S.R. Ahl, P.K. Cook, C. Detlefs, J. Appl. Crystallogr. 50 (2017) 1441–1456.
[15] European Standard for Wheels EN 13262–Product Requirements, 2009.
[16] M. Kutsal, P. Bernard, G. Berruyer, P.K. Cook, R. Hino, A.C. Jakobsen, W. Ludwig, J. Ormstrup, T. Roth, H. Simons, K. Smets, J. Sierra, J. Wade, P. Wattecamps, C. Yildirim, H.F. Poulsen, C. Detlefs, IOP Conf. Ser. Mater. Sci. Eng. 580 (2019) 012007.
[17] T.N.T. Thi, J. Morse, D. Caliste, B. Fernandez, D. Eon, J. Hartwig, C. Barbay, C. Mer-Calfati, N. Tranchant, J.C. Arnault, T.A. Lafford, J. Baruchel, J. Appl. Crystallogr. 50 (2017) 561–569.
[18] H.K.D.H. Bhadeshia, S.A. David, J.M. Vitek, R.W. Reed, Mater. Sci. Technol. 7 (1991) 686–698.
[19] K. Hlushko, J. Keckes, G. Ressel, J. Pörnbacher, W. Ecker, M. Kutsal, P.K. Cook, C. Detlefs, C. Yildirim, Scr. Mater. 187 (2020) 402–406.
[20] B.L. Bramfitt, A.R. Marder, A transmission-electron-microscopy study of the substructure of high-purity pearlite, Metallography, 6, 6th, Elsevier, 1973, pp. 483–495.
[21] D.W. Suh, C.S. Oh, H.N. Han, S.J. Kim, Acta Mater. 55 (2007) 2659–2669.
[22] Y.B. Zhang, T. Andriollo, S. Fæster, W. Liu, J. Hattel, R.I. Barabash, Acta Mater. 121 (2016) 173–180.
[23] V.M. Yershov, Phys. Met. Metallogr. 52 (1981) 90–94.
[24] H.K.D.H. Bhadeshia, Int. Mater. Rev. (2019) 1–27.
[25] E.U. Lee, Metall. Trans. A 23A (1992) 2205–2210.
[26] S. Denis, S. Sjostrom, A. Simon, Metall. Trans. A Phys. Metall. Mater. Sci. 18 A (1987) 1203–1212.
[27] A. Durgaprasad, S. Giri, S. Lenka, S. Kundu, S. Chandra, S. Mishra, R.D. Doherty, I. Samajdar, Metall. Mater. Trans. A Phys. Metall. Mater. Sci. 49 (2018) 1520–1535.
[28] A.R. Marder, B.L. Bramfitt, Metall. Trans. A 6 (1975) 2009–2014.
[29] Y.B. Zhang, T. Andriollo, S. Fæster, R. Barabash, R. Xu, N. Tiedje, J. Thorborg, J. Hattel, D. Juul Jensen, N. Hansen, Acta Mater. 167 (2019) 221–230.
[30] F.R.N. Nabarro, Z.S. Basinski, D.B. Holt, The Plasticity of Pure Single Crystals, 1964.
[31] M.F. Ashby, Philos. Mag. 21 (1970) 399–424.
[32] Y. Wang, T. Ohnuki, Y. Tomota, S. Harjo, T. Ohmura, Scr. Mater. 140 (2017) 45–49.
[33] E.C. Oliver, M.R. Daymond, P.J. Withers, Acta Mater. 52 (2004) 1937–1951.
[34] A. Durgaprasad, S. Giri, S. Lenka, S. Kundu, S. Mishra, S. Chandra, R.D. Doherty, I. Samajdar, Acta Mater. 129 (2017) 278–289.
[35] A. Durgaprasad, S. Giri, S. Lenka, S. Kundu, S. Mishra, S. Chandra, R.D. Doherty, I. Samajdar, Metall. Mater. Trans. A Phys. Metall. Mater. Sci. 48 (2017) 4583–4597.
[36] S. Denis, E. Gautier, S. Sjöström, A. Simon, Acta Metall. 35 (1987) 1621–1632.
[37] K.T. Murray, A.F. Pedersen, I. Mohacsi, C. Detlefs, A.J. Morgan, M. Prasciolu, C. Yildirim, H. Simons, A.C. Jakobsen, H.N. Chapman, H.F. Poulsen, S. Bajt, Opt. Express 27 (2019) 7120.
[38] C. Yildirim, H. Vitoux, L.E. Dresselhaus-Marais, R. Steinmann, Y. Watier, P.K. Cook, M. Kutsal, C. Detlefs, AIP Publishing LLC, Rev. Sci. Instrum. 91 (6) (2020) 065109.